An Integrated Altitude Control Design for a Tail-Sitter UAV Equipped With Turbine Engines

HUANYU LI[1], CHUNWEN LI[1], HANGYU LI[2], YINGJIE LI[1], AND ZHIPENG XING[1]
[1]Department of Automation, Tsinghua University, Beijing 100084, China
[2]Department of Energy Resources Engineering, Stanford University, Stanford, CA 94305, USA

Corresponding author: Huanyu Li (lihuanyu12@mails.tsinghua.edu.cn)

ABSTRACT An accurate and robust altitude controller is critical for vertical takeoff and landing (VTOL) unmanned aerial vehicles (UAVs) in achieving quasi-stationary flight. Most UAV altitude control designs neglect the rotor dynamics. Therefore, they cannot be used for a tail-sitter UAV equipped with turbine engines because of the complicated engine dynamics with an apparent time delay. In this paper, we develop an integrated altitude controller that considers the engine dynamics. The new controller consists of a proportional-derivative (PD) control term and an acceleration feedback term. The stability region in the parameter space is analyzed and the controller is designed to achieve specific gain and phase margins. A UAV hover flight experiment is conducted and the results are presented to demonstrate the effectiveness of the proposed altitude controller.

INDEX TERMS Tail-sitter UAV, turbine engine, time delay, altitude control, acceleration feedback.

I. INTRODUCTION

In recent years, VTOL UAVs become very attractive due to their ability to perform quasi-stationary flight (hover or near hover flight), which enables their application to special missions such as monitoring and inspection for both military and civil uses [1]. An accurate and robust altitude controller is critical for VTOL UAVs to achieve a quasi-stationary flight [2].

A lot of work has been done to address the altitude control problem for VTOL UAVs under quasi-stationary flight conditions. For example, Herisse *et al.* [3] developed a proportional-integral (PI) altitude controller for an electric quadrotor UAV. A stability analysis of their altitude controller was performed, and the hover flight experiment results were given. Another example is the work by Azinheira and Moutinho, who investigated a backstepping-based hover flight controller for a remote monitoring airship UAV [4]. The global asymptotic stability of the UAV was demonstrated in their work, although only simulation results were presented. Later, Lee *et al.* [5] proposed an altitude controller based on dynamic surface control theory for an electric quadrotor UAV. They performed both numerical simulations and experiments, which demonstrated the effectiveness of their controller. In addition, Min *et al.* [6] developed an adaptive

robust altitude controller for a quadrotor-type UAV, although only simulation results were presented. Other examples of UAV altitude control can be found in [7]–[11]. However, all the controllers in the work described above suffer from an important limitation: they all neglect the actual rotor dynamics, which means that they all assume that the desired thrust can be achieved immediately. Although some of the above controllers were applied to real UAV platforms, this important limitation could hinder their use to more complicated UAVs.

Limited work has been done on UAV altitude control while considering rotor dynamics. Here, we select two of the most relevant works for discussion. Besnard *et al.* [12] developed a cascade control framework for a quadrotor UAV. Although the rotor dynamics were considered in their control design, it was assumed that the rotor dynamics are much quicker than the airframe dynamics. In addition, they did not perform stability analysis due to the complicated structure of their controller. Moreover, only the numerical simulation results were presented. A more relevant work is the study by Kita *et al.* [13], who developed a two-stage altitude controller for a tail-sitter VTOL UAV equipped with an electric propeller. The controller consists of a proportional-integral-derivative (PID) controller and a PI controller. Although the structure of this controller is simpler than that in [12], no sta-

bility analysis was conducted to guide the control parameter selection. Consequently, to obtain the control parameters used in their experiment, a simulation-based parameter-tuning process had to be performed, which was time consuming.

In this work, we investigate the altitude control design for a tail-sitter VTOL UAV equipped with turbine engines. In contrast to the electric motors used in previous UAVs, the propulsion system of our UAV is more powerful and can enable a wider range of applications for this type of UAV. However, the dynamic system of the turbine engines is more complicated than the above-mentioned electric motors, and the system has an apparent time delay. Therefore, the engine dynamics cannot be neglected in the altitude control design. We therefore design an integrated controller that considers the engine dynamics. In this control design, the rotor speed command is the control input. This is different from previous control designs in which the thrust force is the control input. The proposed controller consists of a PD control term and an acceleration feedback term. A stability analysis is performed and can be used to guide the parameter selection for the UAV experiment. In addition, the controller is also designed to achieve specific gain and phase margins. We conduct UAV experiments to demonstrate the effectiveness of our integrated controller. To the best of our knowledge, the altitude control and the stability analysis for this type of UAV have not been considered before.

This paper is organized as follows. In Section II, the configuration of the tail-sitter UAV will be introduced. In Section III, the integrated altitude model for UAV quasi-stationary flight will be discussed. In Section IV, the altitude control scheme is proposed and analyzed. The experimental results will be presented in Section V. Finally, we conclude the paper in Section VI.
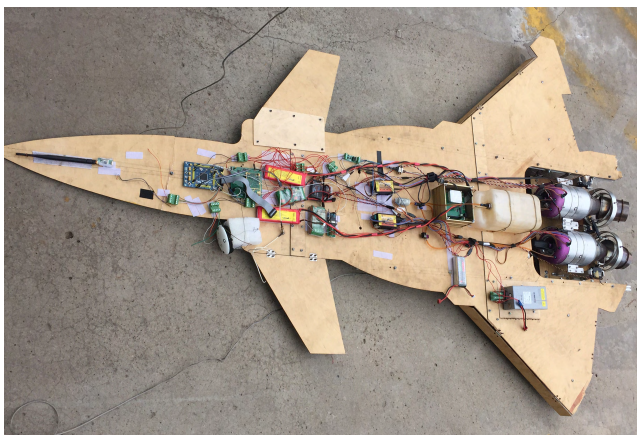

FIGURE 1. The tail-sitter UAV equipped with turbine engines.

II. UAV CONFIGURATION

A new prototype tail-sitter VTOL UAV has been developed at Tsinghua University as shown in Figure 1. The UAV is equipped with two Jetcat P200 micro turbine engines. Each engine is able to provide a maximum thrust of 230 N at a max-

imum rotor speed of 112,000 revolutions per minute (RPM). With two engines, the UAV has a maximum thrust of 460 N, which corresponds to a takeoff mass of approximately 46 kg. The length of the UAV (from nose to tail) is close to 2 m, and the wingspan is approximately 1.6 m. The overall weight (including the engines) of the UAV is approximately 23 kg, depending on the amount of fuel carried.

The UAV is also equipped with a micro-computer, an inertial measurement unit (IMU), a Hall sensor and a laser range finder. The micro-computer controls the UAV by processing all the measured data and providing commands to the engines. The IMU (Analog Devices ADIS16488A) measures the attitude and acceleration of the UAV and provides the data to the micro-computer at a frequency of 25 Hz. The IMU is installed at the center of gravity of the UAV to prevent the rotation (due to external disturbance) of the UAV body from influencing the acceleration measurement. The Hall sensor measures the engine rotor speed with high accuracy (error range of ± 10 RPM for a rotor speed of over 80,000 RPM). The laser range finder (Dimetix DLSB-15) measures the altitude (height above the ground) of the UAV at a frequency of 5 Hz, and it has a measurement error of less than ± 1.5 mm.

III. MODELING

The translational dynamic equation of the UAV in the vertical direction can be written as follows:

$$m\ddot{z}(t) = F_z(t) - mg, \qquad (1)$$

where m is the mass of the UAV, $z(t)$ is the altitude as a function of time t, $F_z(t)$ is the non-gravitational resultant force in the vertical direction, and g is the gravitational acceleration. Under quasi-stationary flight conditions, the thrust force, which points toward the nose of the UAV body, predominates over the aerodynamic forces [14]. By neglecting the aerodynamic forces, the engine thrust, designated $F_t(t)$, can be regarded as the only non-gravitational force exerted on the UAV. Therefore, $F_z(t)$ is the vertical component of $F_t(t)$. Because the attitude of the UAV body can be effectively controlled to be vertical by a high-gain attitude controller under quasi-stationary flight conditions [1], [3], the engine thrust, $F_t(t)$, can be approximated as in the vertical direction. This results in the following:

$$F_z(t) = F_t(t). \qquad (2)$$

Therefore, equation (1) can be rewritten as follows:

$$m\ddot{z}(t) = F_t(t) - mg. \qquad (3)$$

A. ENGINE MODEL

Our previous work has shown that the overall engine model can be divided into two components: a linear dynamic model (rotor speed model), which characterizes the linear relationship between the rotor speed command and the rotor speed response, and a nonlinear static model (thrust model), which characterizes the nonlinear relationships between the rotor speed response and the engine thrust response.

A detailed derivation and description of the engine model can be found at [15] and [16]. In this work, we use the model directly. The two components of the engine model are given by the following:

$$\begin{cases} \dot{\Omega}(t) = K(\Omega_\delta(t - T_D) - \Omega(t - T_D)), \\ F_e(t) = a_3\Omega(t)^3 - a_2\Omega(t)^2 + a_1\Omega(t) - a_0, \end{cases} \quad (4)$$

where $\Omega(t)$ represents the rotor speed response, $\Omega_\delta(t)$ denotes the rotor speed command, T_D is the time delay of the rotor speed model, K is the proportional coefficient, a_3, a_2, a_1 and a_0 are the polynomial coefficients of the nonlinear thrust model, and $F_e(t)$ is the thrust force of a single turbine engine.

As mentioned before, the UAV is equipped with two turbine engines with the same specification. Because they receive the same rotor speed command, the two engines operate at the same rotor speed and generate the same thrust force. Therefore, we have the following:

$$F_t(t) = 2F_e(t). \quad (5)$$

We now introduce another term, F_{e0}, to represent the single-engine thrust at which the UAV is at the equilibrium point ($\ddot{z}(t) = 0$). Under such conditions, the total engine thrust (from the two engines) equals the gravitational force of the UAV. Therefore, we should have $F_{e0} = mg/2$. The corresponding equilibrium rotor speed, designated Ω_0, can be defined as follows:

$$a_3\Omega_0{}^3 - a_2\Omega_0{}^2 + a_1\Omega_0 - a_0 = F_{e0}. \quad (6)$$

We then linearize the engine thrust model, equation (4b), at the equilibrium rotor speed as follows:

$$F_e(t) = F_{e0} + K_e(\Omega(t) - \Omega_0), \quad (7)$$

where $F_{e0} = mg/2$ and

$$\begin{aligned} K_e &= \left.\frac{dF_e(t)}{d\Omega}\right|_{\Omega(t)=\Omega_0} \\ &= (3a_3\Omega_0{}^2 - 2a_2\Omega_0 + a_1). \end{aligned} \quad (8)$$

By substituting (5) and (7) into (4), we get the following:

$$\begin{cases} \dot{\Omega}(t) = K(\Omega_\delta(t - T_D) - \Omega(t - T_D)), \\ F_t(t) = mg + 2K_e(\Omega(t) - \Omega_0). \end{cases} \quad (9)$$

B. INTEGRATED ALTITUDE MODEL

By combining (9) with (3), we can obtain the following:

$$\begin{cases} \dot{\Omega}(t) = K(\Omega_\delta(t - T_D) - \Omega(t - T_D)), \\ m\ddot{z}(t) = 2K_e(\Omega(t) - \Omega_0). \end{cases} \quad (10)$$

If we define

$$\bar{\Omega}(t) = \Omega(t) - \Omega_0, \quad \bar{\Omega}_\delta(t) = \Omega_\delta(t) - \Omega_0, \quad (11)$$

equation (10) can be rewritten as follows:

$$\begin{cases} \dot{\bar{\Omega}}(t) = K(\bar{\Omega}_\delta(t - T_D) - \bar{\Omega}(t - T_D)), \\ m\ddot{z}(t) = 2K_e\bar{\Omega}(t). \end{cases} \quad (12)$$

Equation (12) can then be transformed into the frequency domain using the Laplace transformation, the results are as follows:

$$\begin{cases} s\bar{\Omega}(s) = K(\bar{\Omega}_\delta(s)e^{-sT_D} - \bar{\Omega}(s)e^{-sT_D}), \\ mz(s)s^2 = 2K_e\bar{\Omega}(s). \end{cases} \quad (13)$$

Based on (13), we can obtain the integrated single-input single-output altitude transfer function model, which characterizes the relationship between the engine rotor speed command and the UAV altitude as follows:

$$z(s) = G(s)\bar{\Omega}_\delta(s), \quad (14)$$

where

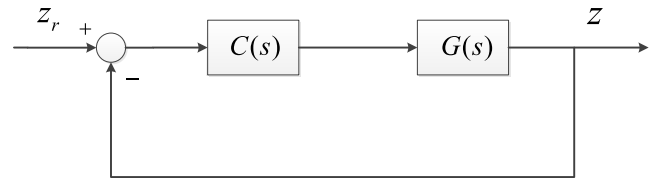$$G(s) = \frac{K_Ge^{-sT_D}}{s^2(s + Ke^{-sT_D})} \text{ with } K_G = \frac{2K_eK}{m}. \quad (15)$$

FIGURE 2. The integrated altitude control system.

IV. CONTROL DESIGN

The integrated altitude control system is shown in Fig. 2, where z_r is the altitude command, z is the UAV altitude response, $C(s)$ is the controller, and $G(s)$ is the altitude transfer function defined in (15). In this paper, we propose a new altitude controller that consists of a PD control term and an acceleration feedback term. The controller can be expressed as follows:

$$C(s) = K_p + K_ds + K_as^2, \quad (16)$$

where $K_p + K_ds$ is the PD control term and K_as^2 is the acceleration feedback term, with K_p, K_d and K_a being the parameters of the controller.

In this section, we will analyze the stability performance of the integrated altitude control system. The controller is also designed to achieve specific gain and phase margins to satisfy the requirement of robustness.

A. STABILITY REGION WITH FIXED k_a

The characteristic equation of the closed-loop integrated control system shown in Fig. 2 can be written as follows:

$$\delta(s) = K_Ge^{-sT_D}(K_p + K_ds + K_as^2) + s^2(s + Ke^{-sT_D}). \quad (17)$$

The closed-loop system is bounded-input bounded-output (BIBO) stable if the characteristic equation, $\delta(s)$, has no roots in the closed right-half of the s-plane [18]. We now analyze the roots of $\delta(s)$. To do that, we define $\delta^*(s)$ as follows:

$$\begin{aligned} \delta^*(s) &= e^{sT_D}\delta(s) \\ &= K_G(K_p + K_ds + K_as^2) + s^2(se^{sT_D} + K) \\ &= s^3e^{sT_D} + k_as^2 + k_ds + k_p, \end{aligned} \quad (18)$$

where $k_a = K + K_G K_a$, $k_d = K_G K_d$, and $k_p = K_G K_p$. Note that K and K_G are the parameters of the UAV engine model, and they are constant for a particular UAV.

Because there are no finite zeros of e^{sT_D}, the roots of $\delta^*(s)$ are identical to those of $\delta(s)$ [19]. Therefore, we study the roots of $\delta^*(s)$ instead of doing that directly on $\delta(s)$.

According to the D-partition theory [20], the boundaries between the stable and unstable parameter regions consist of three parts: the real root boundary (RRB) defined by $\delta^*(0) = 0$, the infinite root boundary (IRB) defined by $\delta^*(\infty) = 0$, and the complex root boundary (CRB) defined by $\delta^*(jw) = 0$ for $w \in (-\infty, 0) \cup (0, \infty)$ by letting $s = jw$.

One can easily find that the IRB does not exist for the characteristic equation described in (18) according to [21]. The following discussion will be focused on the RRB and the CRB.

The RRB requires $\delta^*(0) = 0$. Based on (18), we can easily obtain the RRB as follows:

$$k_p = 0. \qquad (19)$$

To obtain the CRB, we need to investigate $\delta^*(jw) = 0$ for $w \in (-\infty, 0) \cup (0, \infty)$. Because the parameters of the characteristic equation are real, if $s = jw$ is a root of the characteristic equation, so is its complex conjugate ($s = -jw$). Therefore, it is sufficient to consider $\delta^*(jw) = 0$ for $w \in (0, \infty)$ to compute the CRB. By substituting $s = jw$ into (18), the equation can then be rewritten as follows:

$$\delta^*(jw) = \delta_r(w) + j\delta_i(w), \qquad (20)$$

with $\delta_r(w)$ and $\delta_i(w)$ represent the real and imaginary parts of $\delta^*(jw)$, respectively, and they are expressed as follows:

$$\begin{cases} \delta_r(w) = w^3 sin(wT_D) - k_a w^2 + k_p, \\ \delta_i(w) = -w^3 cos(wT_D) + k_d w. \end{cases} \qquad (21)$$

Both $\delta_r(w) = 0$ and $\delta_i(w) = 0$ are needed to have $\delta^*(jw) = 0$. Therefore, the solution of the CRB is expressed as follows:

$$\begin{cases} k_d = w^2 cos(wT_D), \\ k_p = -w^3 sin(wT_D) + k_a w^2. \end{cases} \qquad (22)$$

From (22), it can be seen that k_d and k_p are functions of k_a and w. By fixing k_a, we are able to obtain the CRB curve $(k_d(w), k_p(w))$ in the k_d-k_p plane with w varying from 0 to ∞.

We now present an example to show the RRB and CRB curves in the k_d-k_p plane for $k_a = 3.6$. As shown in Fig. 3, the red line indicates the RRB line, while the blue line indicates the CRB curve. The stability region, if it exists, will be bounded by the two curves. In the calculation of the CRB curve, a time delay of 0.28 s ($T_D = 0.28$) for the turbine engine is used. This time delay was identified in our previous work [15], and here, we use it directly.

After obtaining the RRB and CRB curves in the k_d-k_p plane, we need to determine which side of the curves the stability region falls onto. For the CRB, the following proposition is used [23]: the stability region must be on the right-hand
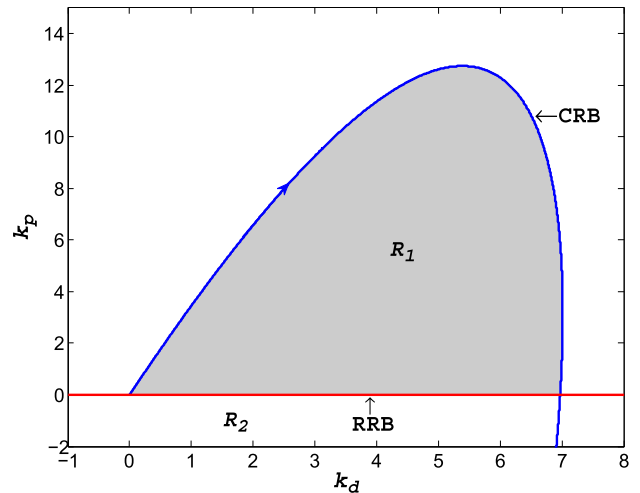

FIGURE 3. The RRB and CRB curves and the stability region in the k_d-k_p plane for $k_a = 3.6$.

side of the CRB curve following the curve in the direction of increasing w if $detJ < 0$; otherwise, the stability region must be on the left-hand side of the CRB curve, where J is the Jacobian matrix defined as follows:

$$J = \begin{bmatrix} \dfrac{\partial \delta_r(s)}{\partial k_d} & \dfrac{\partial \delta_r(s)}{\partial k_p} \\ \dfrac{\partial \delta_i(s)}{\partial k_d} & \dfrac{\partial \delta_i(s)}{\partial k_p} \end{bmatrix}_{(k_p,k_d,k_a,T_D,w).} \qquad (23)$$

In this work, $detJ = -w < 0$ because we consider $w \in (0, \infty)$. Therefore, the stability region must be on the right-hand side of the CRB curve in the k_d-k_p plane following the curve in the direction of increasing w which is indicated by the arrow in Fig. 3.

Now, we need to determine which side of the RRB line the stability region falls onto. There are two regions (R_1 and R_2) separated by the RRB line, as shown in Fig. 3. Both regions are on the right-hand side of the CRB curve, which means that they both satisfy the CRB stability criterion. Because there is no analytical method to determine the stability region for the RRB line, a numerical test is needed. To this end, we need to select a random test point in R_1 and another test point in R_2, and we apply the method developed in [24]. The region to which the stable test point belongs is the stability parameter region. In this work, we identified the shaded area R_1, which is above the RRB line, as the stability region for our control system.

B. STABILITY RANGE OF k_a

In the previous section, we computed the stability region in the k_d-k_p plane for $k_a = 3.6$. If we then vary the value of k_a, we will obtain different sets of RRB and CRB curves and the corresponding stability regions. The new stability regions may be of different size or shape compared with the stability region shown in Fig. 3. For certain k_a values, the stability region may vanish. We now investigate the upper and lower limits of k_a with which the stability region exists.
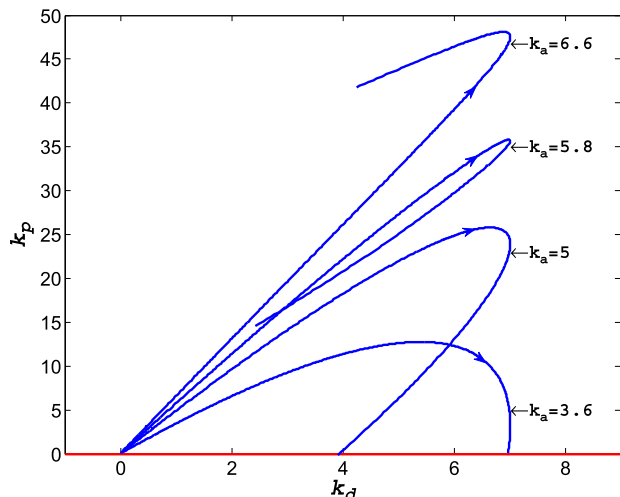
FIGURE 4. The RRB and CRB curves for larger k_a values.

FIGURE 5. The derivatives of k_p and k_d for larger k_a values.

1) UPPER LIMIT OF k_a

We first perform a numerical experiment to understand how the stability region changes with increasing k_a. The case with $k_a = 3.6$ is considered as the base case. We increase k_a to higher values ($k_a = 5$, 5.8 and 6.6) and compute the corresponding RRB and CRB curves in the k_d-k_p plane. The results are shown in Fig. 4. The RRB lines for those higher k_a values are identical, and they all overlap with the k_d-axis. The curves with arrows are the CRB curves, and those arrows again indicate the direction of increasing w. The stability region for $k_a = 5$, although not shown explicitly in the figure, is still the confined area bounded by the RRB line and the CRB curve. However, this stability region is of a different shape compared with the stability region for $k_a = 3.6$. It has a higher maximum k_p value but a smaller nonzero intersection between the CRB curve and the RRB line on the k_d-axis. If we further increase k_a to 5.8, it can be seen that the CRB curve intersects itself before crossing the RRB line. In this situation, the stability region is only bounded by the CRB curve, and the region is much smaller. If we then increase k_a to 6.6, we can see that the confined area on the right-hand side of the CRB curve (following the direction of increasing w) does not exist. This means that there is no stability region for $k_a = 6.6$.

Based on the numerical experiment, we can see that the CRB curve strongly impacts the stability region. We now derive the theoretical upper limit of k_a by analyzing the CRB curve. According to (22), we can compute the following:

$$\begin{cases} \dfrac{dk_d}{dw} = -w^2 T_D \sin(wT_D) + 2w\cos(wT_D), \\ \dfrac{dk_p}{dw} = -w^3 T_D \cos(wT_D) - 3w^2 \sin(wT_D) + 2k_a w. \end{cases} \quad (24)$$

For the k_a values considered in Fig. 4, we can plot the dk_d/dw and dk_p/dw curves in Fig. 5. Because dk_d/dw is independent of k_a, all the dk_d/dw curves collapse to one line (red line). Here, we only plot a small portion of the dk_d/dw and dk_p/dw curves. All curves will extend to below the w-axis (negative
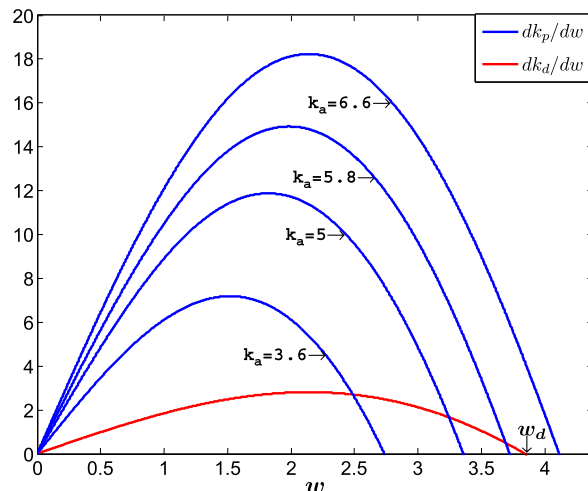
derivative) after crossing the w-axis. Those curves are not shown in Fig. 5 because they are irrelevant to our discussion. By defining w_d as the minimum positive value, which satisfies

$$\left.\frac{dk_d}{dw}\right|_{w=w_d} = 0, \quad (25)$$

and w_p as the minimum positive value, which satisfies

$$\left.\frac{dk_p}{dw}\right|_{w=w_p} = 0, \quad (26)$$

we will have $dk_d/dw > 0$ for $w \in (0, w_d)$, and $dk_p/dw > 0$ for $w \in (0, w_p)$. This indicates that k_d is at its local maximum at $w = w_d$ and that k_p is at its local maximum at $w = w_p$.

We first assume that $w_p < w_d$, and it is easy to obtain the following:

$$\begin{cases} \dfrac{dk_d}{dw} > 0, \dfrac{dk_p}{dw} > 0, & \text{for } w \in (0, w_p), \\ \dfrac{dk_d}{dw} > 0, \dfrac{dk_p}{dw} < 0, & \text{for } w \in (w_p, w_d). \end{cases} \quad (27)$$

According to the implicit function theorem, for $w \neq w_d$, the slope of the CRB curve can be written as follows:

$$\frac{dk_p}{dk_d} = \frac{dk_p}{dw} \Big/ \frac{dk_d}{dw}. \quad (28)$$

For $w \in (0, w_p)$, both dk_d/dw and dk_p/dw are positive. This results in an increase in k_d and k_p values with the increase in w, and the slope of the CRB curve is positive until k_p reaches its local maximum at w_p. For $w \in (w_p, w_d)$, k_p starts to decrease with the increase in w, while k_d still increases. The slope of the CRB curve becomes negative, and the CRB curve "turns to the right" sharply following the direction of increasing w until k_d reaches its maximum at w_d (see the CRB curve for $k_d = 3.6$ in Fig. 4). When w further increases to greater than w_d, both k_d and k_p will decrease with increasing w. The CRB curve will continue "turning to

the right''. Depending on the value of k_a, the CRB curve will either cross the RRB line (k_d-axis) at first or cross itself at first (see the CRB curves for $k_a = 5$ and $k_a = 5.8$ in Fig. 4). In either situation, a confined area will form on the right-hand side of the CRB curve following the direction of increasing w, and this area is above the RRB line. Therefore, this confined area is the stability region of our control system.

However, if $w_p > w_d$, we will have:

$$\begin{cases} \dfrac{dk_d}{dw} > 0, \dfrac{dk_p}{dw} > 0, & \text{for } w \in (0, w_d), \\ \dfrac{dk_d}{dw} < 0, \dfrac{dk_p}{dw} > 0, & \text{for } w \in (w_d, w_p). \end{cases} \quad (29)$$

As a result, k_d reaches its local maximum first at $w = w_d$. After that, k_d starts to decrease, while k_p continues increasing until k_p reaches its local maximum at $w = w_p$. Because of this, the CRB curve will "turn to the left" sharply at $w = w_d$. In this situation, there is no confined area on the right-hand side of the CRB curve following the direction of increasing w, i.e., the stability region does not exist (see CRB curve for $k_a = 6.6$ in Fig. 4).

Based on the above analysis, we can see that the magnitude of w_p relative to w_d determines whether the stability region exists. When $w_p < w_d$ (for cases with $k_a = 3.6, 5$ and 5.8), the stability region exists. By contrast, when $w_p > w_d$ (for the case with $k_a = 6.6$), the stability region does not exist. The boundary corresponds to the condition of $w_p = w_d$.
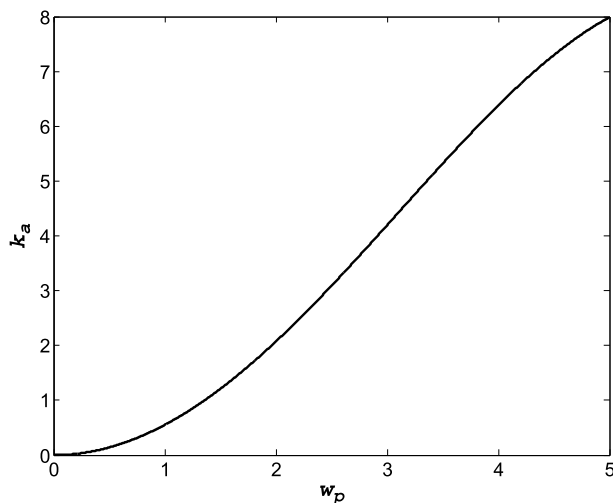

FIGURE 6. Relationship between k_a and w_p.

According to (24), w_d is independent of k_a, while w_p depends on k_a. By substituting (26) into (24), we can obtain the relationship between k_a and w_p as follows:

$$k_a = \frac{1}{2}[w_p^2 T_D cos(w_p T_D) + 3w_p sin(w_p T_D)]. \quad (30)$$

We then plot k_a as a function of w_p for $w_p \in (0, 5)$ in Fig. 6. As can be seen, k_a monotonically increases with increasing w_p. Therefore, the upper limit of w_p also corresponds to the upper limit of k_a. By substituting $w_p = w_d$ into (30),

we obtain the following:

$$k_{au} = \frac{1}{2}[w_d^2 T_D cos(w_d T_D) + 3w_d sin(w_d T_D)], \quad (31)$$

where k_{au} is the upper limit of k_a. An easy way of solving this equation is to compute $w_d T_D$ at first by combining (24) and (25), which gives us the following:

$$w_d T_D tan(w_d T_D) = 2. \quad (32)$$

By applying the numerical solution method, we obtain $w_d T_D = 1.08$. We then substitute this into (31) and obtain the following:

$$k_{au} = 1.70/T_D. \quad (33)$$

As mentioned previously, $T_D = 0.28$. Therefore, we finally obtain $k_{au} = 6.06$, which is the upper limit of k_a above which the stability region does not exist for the altitude controller.

2) LOWER LIMIT OF k_a

We now investigate the lower limit of k_a below which the stability region does not exist. Similar to the previous discussion, we reduce k_a from 3.6 and compute the RRB and CRB curves for the smaller k_a values. The results are shown in Fig. 7. It can be seen that as k_a decreases, the stability region shrinks. Eventually, when $k_a = -0.2$, the stability region vanishes because the area on the right-hand side of the CRB curve (following the direction of increasing w) is below the RRB line. In the following discussion, we will prove that the lower limit of k_a is zero.
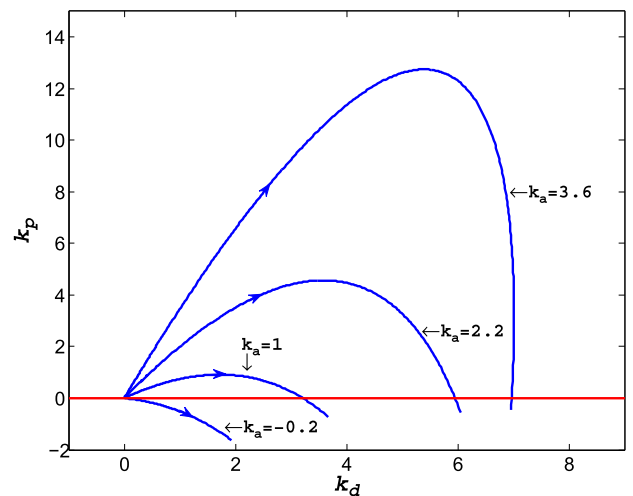

FIGURE 7. The RRB and CRB curves for smaller k_a values.

According to (24), for cases in which k_a is equal to or less than zero, dk_p/dw is negative when w begins to increase from zero (see the dk_p/dw curve for $k_a = -0.2$ in Fig. 8). This means that the CRB curve will go directly below the RRB line, as can be seen in the CRB curve for $k_a = -0.2$ in Fig. 7. Under this condition, the stability region does not exist. Note that the dk_d/dw curve is unchanged, and it is positive for $w < w_d$.
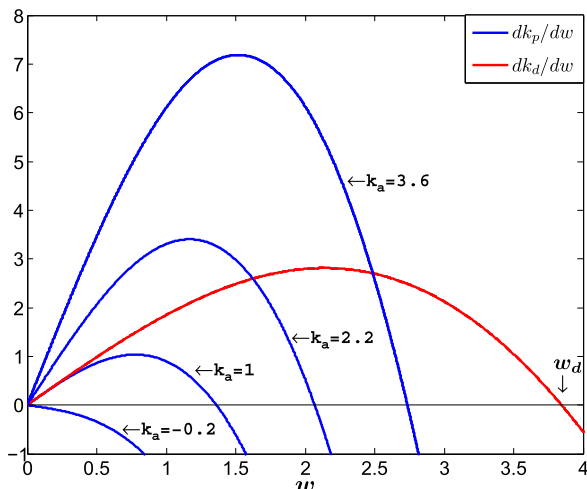
FIGURE 8. The derivatives of k_p and k_d for smaller k_a values.

However, if k_a is greater than zero, regardless of how small k_a is, we will have $w_p > 0$ according to (30) and Fig. 6. Based on previous analysis, we have $w_p < w_d$ when k_a is very small ($k_a < k_{au}$). For the same as equation (27), we have the following:

$$\begin{cases} \dfrac{dk_d}{dw} > 0, \dfrac{dk_p}{dw} > 0, & \text{for } w \in (0, w_p), \\ \dfrac{dk_d}{dw} > 0, \dfrac{dk_p}{dw} < 0, & \text{for } w \in (w_p, w_d). \end{cases} \quad (34)$$

In this situation, k_p reaches its local maximum at $w = w_p$, which occurs earlier than k_d reaching its local maximum at $w = w_d$. As a result, the CRB curve will extend in the upper-right direction from the origin and "turn to the right" to cross the RRB line, which will form a stability region.

From the above analysis, we can conclude that the lower limit of k_a is zero to allow the stability region to exist. Therefore, the range of k_a should be $0 < k_a < k_{au}$ to achieve a stable altitude control.

3) WHY ACCELERATION FEEDBACK IS NEEDED
As defined before, $k_a = K + K_G K_a$, where K and K_G are the parameters of the UAV and K_a is the coefficient of the acceleration feedback term. If we do not consider the acceleration feedback, the K_a coefficient should equal zero. Therefore, we will have $k_a = K$. The altitude controller reduces to a PD controller. For our UAV, $K = 3.0881$, which means that $k_a = 3.0881$. This k_a value is still within the stability range of k_a computed above ($0 < k_a < 6.06$). This indicates that there exists a stability region for the reduced PD controller.

However, as shown in (33), the upper limit of k_a depends on the time delay T_D. For UAVs with turbine engines or other propulsion systems with a larger T_D, the k_a range can be significantly reduced. For example, if T_D is doubled, the upper limit of k_a for a stable UAV altitude control will be reduced to 3.03. In this situation, the stability region will not exist

for the PD controller because $k_a = 3.0881$ is outside of the stability range.

With the added acceleration feedback term, we can adjust the K_a coefficient to let k_a fall within the k_a stability range. This means that the new controller developed in this work is able to achieve stable altitude control with much greater time delay in the engines.

C. GAIN AND PHASE MARGINS
In reality, the UAV control performance is inevitably influenced by external disturbances and the control model uncertainties. The control system needs to be sufficiently robust to ensure a successful flight. The gain margin and the phase margin are two important measures for quantifying the robustness of a control design [25]. We need to design our controller to achieve certain gain and phase margins.
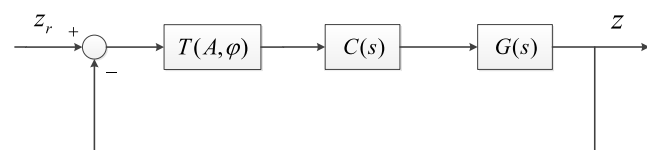

FIGURE 9. The altitude control system with the gain-phase margin tester.

The altitude control system with the gain-phase margin tester, $T(A, \varphi)$, is shown in Fig. 9. The tester is typically expressed by the following:

$$T(A, \varphi) = A e^{-j\varphi}, \quad (35)$$

where A is the gain margin of the system when $\varphi = 0$, and φ is the phase margin of the system when $A = 1$.

The characteristic equation of the closed-loop system in Fig. 9 can be written as follows:

$$\delta_T(s) = A e^{-j\varphi} K_e K e^{-sT_D}(K_p + K_d s + K_a s^2) + s^2(s + K e^{-sT_D}). \quad (36)$$

Similar to what we did for $\delta(s)$ in (17), we define $\delta_T^*(s)$ as follows:

$$\begin{aligned} \delta_T^*(s) &= e^{j\varphi + sT_D}\delta(s) \\ &= A K_e K(K_p + K_d s + K_a s^2) + s^2(se^{j\varphi + sT_D} + Ke^{j\varphi}) \\ &= s^3 e^{j\varphi + sT_D} + s^2(A(k_a - K) + Ke^{j\varphi}) + sAk_d + Ak_p. \quad (37) \end{aligned}$$

By substituting $s = jw$ into (37), we can obtain the real part, $\delta_{Tr}(w)$, and the imaginary part, $\delta_{Ti}(w)$, of $\delta_T^*(s)$ as follows:

$$\begin{cases} \delta_{Tr}(w) = w^3 sin(\varphi + wT_D) - Kw^2 cos(\varphi) + Ak_p, \\ \delta_{Ti}(w) = -w^3 cos(\varphi + wT_D) - Kw^2 sin(\varphi) + Ak_d w. \end{cases} \quad (38)$$

By fixing the value of k_a, we compute the RRB of the system as

$$k_p = 0, \quad (39)$$

and the CRB as

$$\begin{cases} k_d = \dfrac{1}{A}\left[w^2 cos(\varphi + wT_D) + Kw sin(\varphi)\right], \\ k_p = \dfrac{1}{A}\left[-w^3 sin(\varphi + wT_D) + Kw^2 cos(\varphi)\right]. \end{cases} \quad (40)$$

By setting $A > 0$ and $\varphi = 0$, we can plot the gain margin boundaries in the k_d-k_p plane, inside which the altitude control system has a gain margin that is greater than A. By setting $A = 1$ and $\varphi > 0$, we can plot the phase margin boundaries in the k_d-k_p plane, inside which the altitude control system has a phase margin that is greater than φ. The overlap area of the two regions satisfies both criteria. Therefore, the UAV altitude control is said to be robust for parameters chosen inside this region.

In this work, we adopt gain and phase margins based on the work in [18]. The gain margin is chosen as 2, and the phase margin is chosen as 45°. Using $k_a = 3.6$ as our example, the corresponding stability boundaries, gain margin boundaries and phase margin boundaries are shown in Fig. 10. Inside the shaded area **S**, the UAV altitude control system has a gain margin of greater than 2 and a phase margin of greater than 45°.

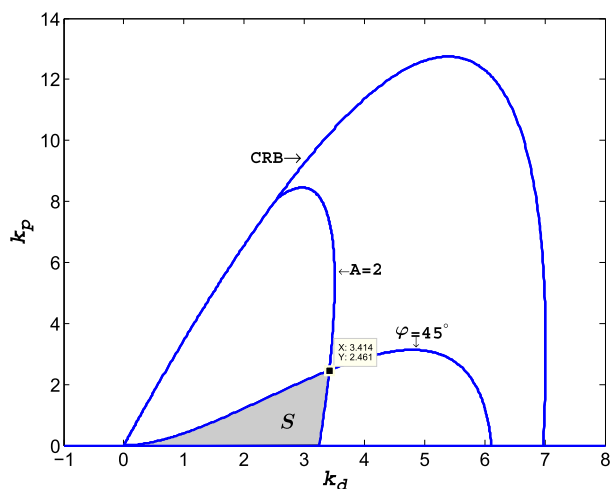**FIGURE 11.** Region *S* for different k_a.

FIGURE 10. Gain-phase margin boundaries for $k_a = 3.6$.

By varying k_a from 2.8 to 4.2 with a step size of 0.2 and repeating the above procedure, a set of region **S** (stability region with a gain margin of greater than 2 and a phase margin of greater than 45°) is obtained and is shown in Fig. 11. From the figure, we can see that region **S** has the largest size for $k_a = 3.6$. Therefore, we use $k_a = 3.6$ in the UAV experiment. After obtaining k_a, we then select k_d and k_p at the point whereby the gain margin CRB curve intersects the phase margin CRB curve (the black point in Fig. 10). The k_d and k_p are computed as 3.414 and 2.461, respectively, and their values are also shown in Fig. 10.

V. EXPERIMENTAL RESULTS

Most VTOL UAVs are equipped with electric motors as discussed in the Introduction section. The structures of those UAVs are relatively simple, and they are typically lightweight. Therefore, the UAV experiments are relatively easy to perform. However, our UAV is equipped with two turbine engines and weights over 20 kg. A control failure during the experiment may result in severe consequences to
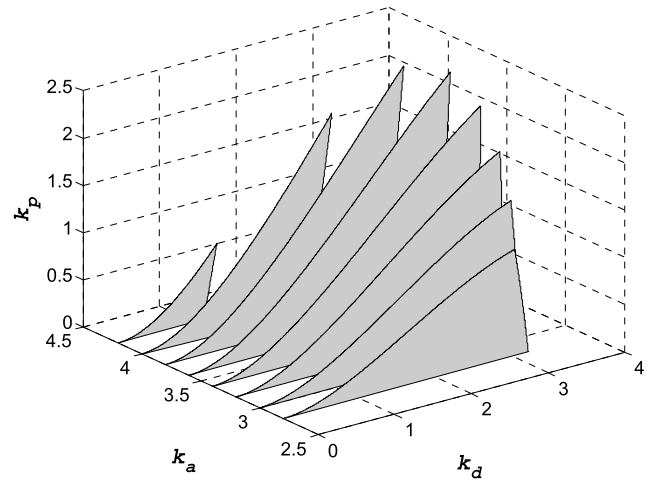
the operating staff and to the UAV itself. For safety considerations, the UAV experiment has to be performed in an open space outdoors. In addition, the UAV does not take off from or land onto the ground directly because that requires a launcher and other auxiliary equipment which can be very complicated to build and very expensive. Instead, our UAV is suspended under a gantry crane using a steel cable (as shown in Fig. 12), and the UAV takes off from the suspended location. The staff and the UAV are protected by the steel cable during the flight experiments. The height of the gantry is 7.2 m, and the width is 6.8 m. When the UAV is suspended, the tail of the UAV is at a height of approximately 1.5 m above the ground to minimize ground effects influencing the engine performance.
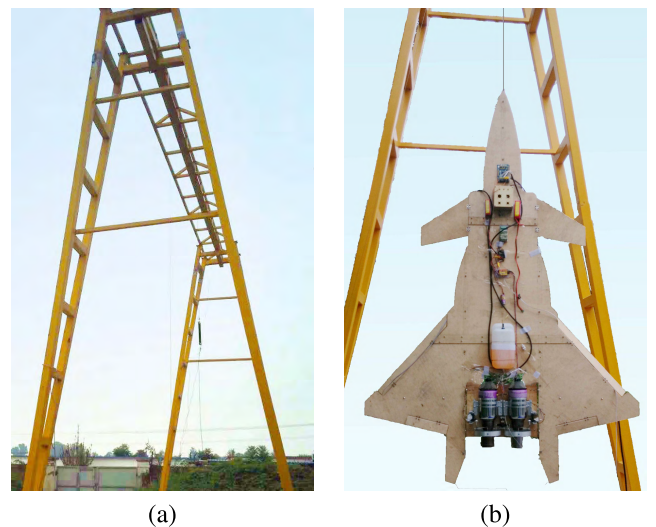

(a)   (b)

FIGURE 12. The experimental platform. (a) Gantry crane; (b) Suspended UAV.

The configuration of the UAV flight experiment system is shown in Fig. 13. The altitude, vertical acceleration and engine rotor speed were measured by the laser range finder,
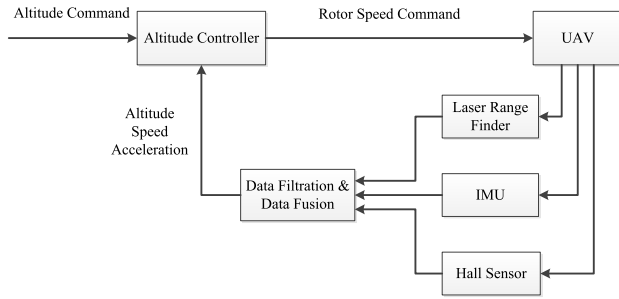
FIGURE 13. The configuration of the UAV flight experiment system.

the IMU and the Hall sensor, respectively. The noise in the acceleration measurement was suppressed by the data filtration method developed in our previous work [16]. A data fusion method was used to estimate the vertical velocity of the UAV by fusing the acceleration measurement with the altitude measurement.

As discussed in the previous section, the following parameters of the altitude controller were adopted: $k_a = 3.6$, $k_d = 3.414$ and $k_p = 2.461$. Using these parameters, we back-calculated the direct control parameters, K_a, K_d and K_p, using the following expressions:

$$\begin{cases} K_a = (k_a - K)/K_G, \\ K_d = k_d/K_G, \\ K_p = k_p/K_G. \end{cases} \tag{41}$$

In this experiment, the UAV had a mass of 22.5 kg, which resulted in an equilibrium engine rotor speed of 86700 RPM ($\Omega_0 = 86700$ RPM). According to (15), K_G was computed as 1.15×10^{-3}. By substituting K_G into (41), we can obtain $K_a = 4.45 \times 10^2$, $K_d = 2.97 \times 10^3$ and $K_p = 2.14 \times 10^3$.

As mentioned before, the UAV was suspended under the gantry crane with a 4 mm stainless steel cable. Initially, the cable was in a tensed condition because it needed to carry the weight of the UAV. After the UAV took off, the cable became loosened because of the elevation change of the UAV. The loosened cable would exert a force on the UAV body due to the weight of the cable. The force in the vertical direction may be neglected compared with the engine thrust force. In addition, our altitude controller is robust enough that the altitude of the UAV was barely impacted. However, the horizontal component of the cable force, in addition to other external disturbances (such as wind), may influence the UAV position in the horizontal plane. In this work, we did not impose horizontal control for our UAV because altitude control is the focus here.

Because of this practical limitation, the UAV may drift horizontally during the hover flight. The distance of the UAV horizontal drifting was constrained by the length of the cable and the height increase of the UAV. The maximum radius, r, for UAV horizontal drifting can be computed as follows:

$$r = \sqrt{l^2 - (l - \Delta h)^2}, \tag{42}$$

where l is the length of the cable, and Δh represents the height

increase of the UAV under the hover flight condition relative to the initial condition.

In the experiment, the altitude (height of the UAV tail above the ground) before takeoff was approximately 1.5 m, and the altitude command was set to be 1.7 m for the hover flight. Therefore, the UAV elevation change was 0.2 m. Because the length of the steel cable was approximately 3.7 m, the maximum radius for the UAV horizontal drifting was computed as 1.2 m according to (42). By increasing Δh (UAV altitude change), the UAV can have a larger horizontal moving space. However, this can result in a safety hazard, because the UAV may hit the crane when a strong engine overshoot occurs. In addition, we sometimes need to switch off the engines in the case of unexpected problems occurring. In such situations, the UAV is more prone to being damaged if it falls from a higher altitude. Therefore, we used $\Delta h = 0.2$ m in this work.

At the beginning of the experiment, the engine rotor speed was controlled manually. The rotor speed command was increased gradually until it reached a value slightly lower than the equilibrium rotor speed (Ω_0). Then, the UAV was switched to automatic control. This process was used to prevent the engine overshoot that could occur if automatic control were to be applied immediately after the engines started.
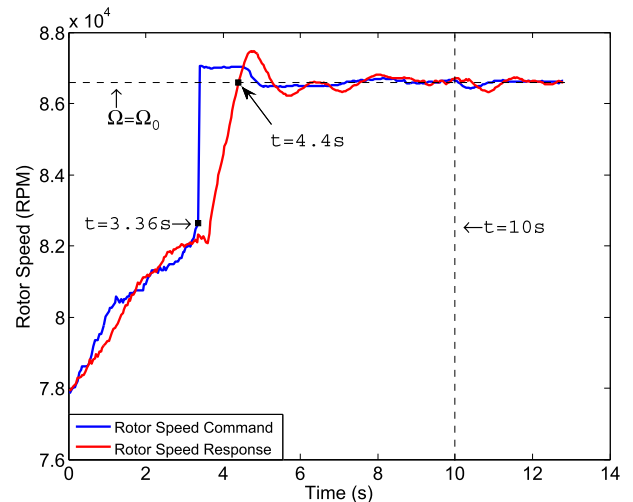

FIGURE 14. The engine rotor speed during the experiment.

We now present the experimental results. Fig. 14 shows the engine rotor speed command and the actual engine rotor speed response during the experiment. Figs. 15-17 show the UAV vertical acceleration, UAV vertical velocity (estimated based on acceleration and altitude measurements) and UAV altitude. Fig. 18 shows the pictures of the UAV status at different times during the experiment. As mentioned before, the engines were manually controlled at the beginning until they reached a rotor speed close to the equilibrium speed. This corresponds to the blue line from 0 s to 3.36 s, as shown in Fig. 14. Because the rotor speed was increased gradually, the rotor speed response (shown in red line in Fig. 14) was close to the command. During this manual control period, the UAV remained stationary because the thrust force was not
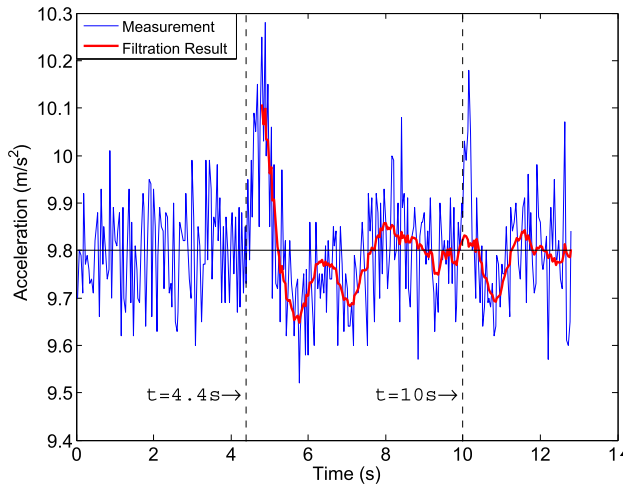
FIGURE 15. The UAV vertical acceleration during the experiment.

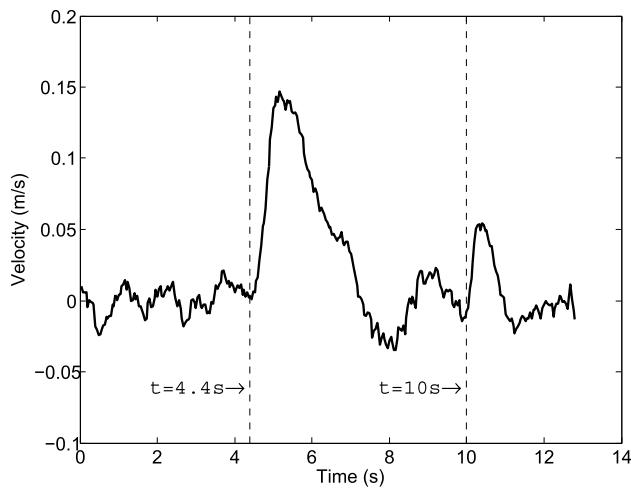**FIGURE 17.** The UAV altitude during the experiment.

FIGURE 16. The UAV vertical velocity during the experiment.

sufficient to lift the UAV. Therefore, the IMU measured the gravitational acceleration, which equals 9.8 m/s^2, as shown in Fig. 15. The noise in the acceleration measurement was the result of many factors such as the vibration of the turbine engines and the external disturbances. Consequently, the UAV vertical velocity presented slight fluctuations about zero (Fig. 16), and the UAV altitude remained at approximately 1.5 m. This period corresponds to the flight status shown in Fig. 18A.

After the engines were switched to automatic control at 3.36 s, there was a sudden increase in the rotor speed command. The rotor speed response also started to increase but only gradually. This resulted in a clear discrepancy between the rotor speed command and the rotor speed response. This discrepancy is why an integrated controller is needed for UAVs equipped with this type of engine. At approximately 4.4 s, the rotor speed response exceeded the equilibrium speed. The UAV started to take off at this time. Thereafter, an apparent increase began to build in the UAV acceleration, UAV velocity and UAV altitude, as shown in Figs. 15-17. Note that a filtration method developed in our previous work
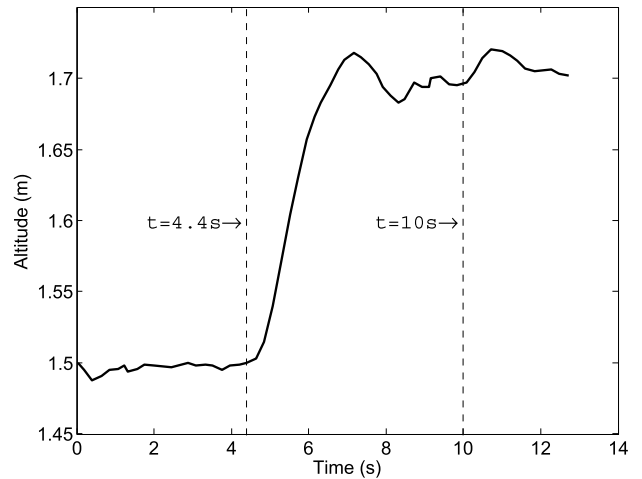
was applied to suppress the noise in the acceleration measurements after the UAV took off, and it took approximately half a second to converge [16]. Therefore, the filtration result of the UAV vertical acceleration (red line in Fig. 15) started at approximately 4.9 s. The filtration result was the acceleration actually used by the controller.

The engines quickly reached their highest rotor speed at approximately 4.8 s and gradually stabilized to very close to the equilibrium rotor speed at approximately 7.5 s. Although there were some fluctuations in the rotor speed response during this period, it quickly converged to the equilibrium speed. After convergence, the UAV was considered to be at the hover flight condition. Consequently, the UAV vertical acceleration was close to the gravitational acceleration, as shown in Fig. 15; the UAV vertical velocity was close to zero, as shown in Fig. 16; and the UAV altitude was at the target altitude (1.7 m), as shown in Fig. 17. The flight status during this period is displayed in Fig. 18B and Fig. 18C. We can see that the UAV was drifting away from the camera in the horizontal plane due to the force exerted by the steel cable and other external disturbances.

Note that at approximately 10 s, the UAV reached its limit for horizontal drifting. The steel cable became tensed again, and it applied both a vertical force (pointing upward) and a horizontal force (pointing toward the camera) to the UAV. Therefore, the UAV moved closer to the camera at 12.5 s, as shown in Fig. 18D. In addition, we can see a sudden increase in the UAV acceleration in Fig. 15. We also observe an increase in the UAV vertical velocity and UAV altitude in Figs. 16 and 17, respectively. These were all caused by the interference of the steel cable. However, the UAV altitude controller quickly responded to this sudden interference and reduced the rotor speed slightly to offset the increase in altitude. Therefore, there was a slight decrease in the rotor speed response after the disturbance, and the UAV altitude quickly returned to 1.7 m. The fluctuation in the UAV altitude was less than ±3 cm after the hover flight condition was
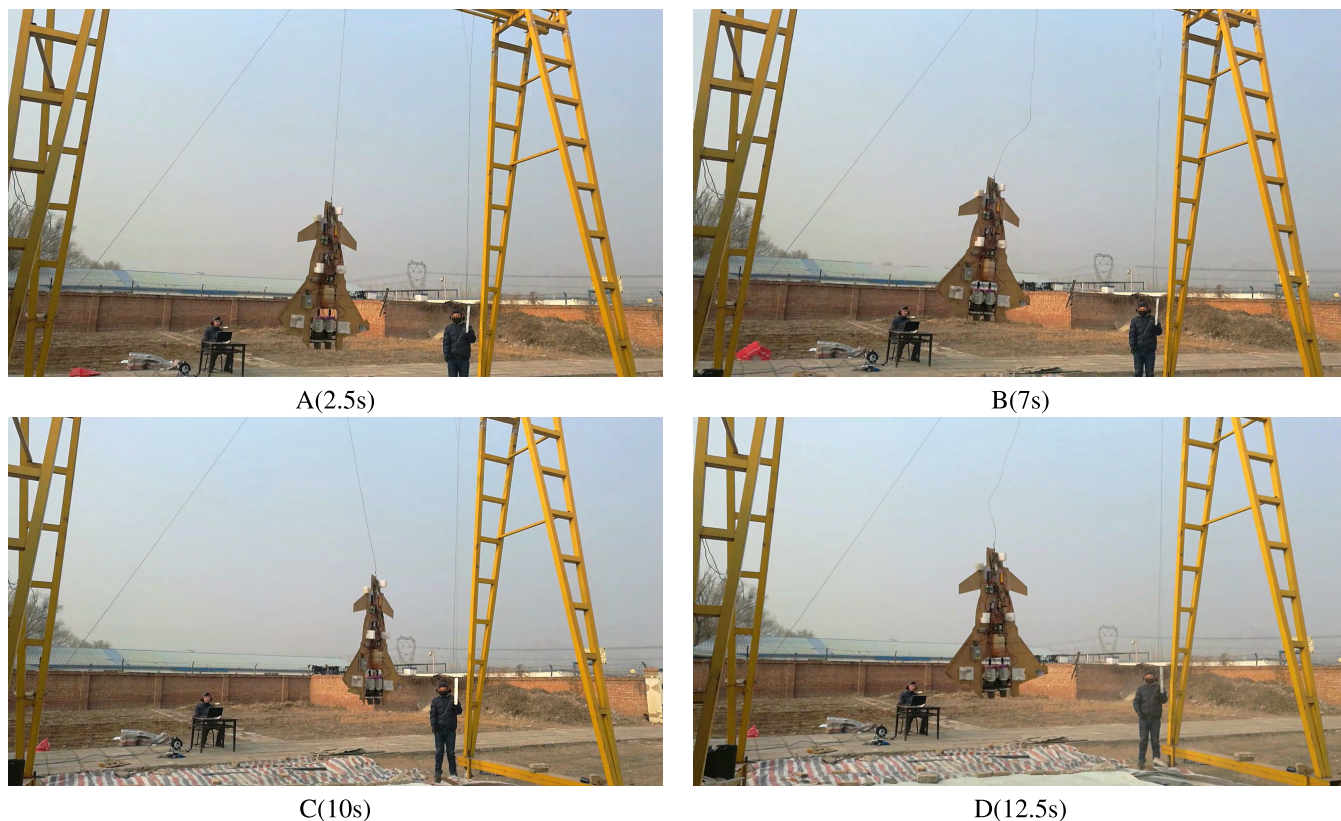
A(2.5s)

B(7s)

C(10s)

D(12.5s)

FIGURE 18. The UAV flight status during the experiment.

reached. This small fluctuation demonstrated the effectiveness of our integrated controller.

VI. CONCLUSION

In this work, we developed an integrated altitude controller for a tail-sitter UAV equipped with turbine engines. The turbine engine dynamics are considered in our control design because the engines have an apparent time delay. The controller consists of a PD control term and an acceleration feedback term. The added acceleration feedback term provides additional flexibility for the control design. To ensure a robust altitude control, the controller is also designed to achieve a gain margin of 2 and a phase margin of 45°.

We performed the stability analysis for the controller and determined the stability region in the parameter space. In addition, a UAV hover flight experiment was conducted using the new altitude controller. Due to the practical constraints, the UAV had to be suspended under a gantry crane using a steel cable, which limited its moving space and produced interference with the UAV during flight. The results of the engine rotor speed, UAV vertical acceleration, UAV vertical velocity and UAV altitude showed that the UAV altitude was effectively controlled at the target altitude, with fluctuations of less than ±3 cm, even with the interference of the steel cable. These results demonstrated the effectiveness of the new altitude controller.

In our current experiment, the UAV exhibited horizontal drifting due to the influence of the steel cable and other external disturbances. This restricted the duration of the flight experiment. Horizontal position control should be added to the UAV control system to limit its horizontal movement. A high-accuracy positioning system is a prerequisite for horizontal position control. This will be considered in our future work. Eventually, a free-flight experiment will need to be conducted to fully test the applicability of our UAV.

REFERENCES

[1] B. Herissé, T. Hamel, R. Mahony, and F.-X. Russotto, "Landing a VTOL unmanned aerial vehicle on a moving platform using optical flow," *IEEE Trans. Robot.*, vol. 28, no. 1, pp. 77–89, Feb. 2012.

[2] A. Dzul, R. Lozano, and P. Castillo, "Adaptive altitude control for a small helicopter in a vertical flying stand," in *Proc. 42nd IEEE Conf. Decision Control*, vol. 3. Dec. 2003, pp. 2710–2715.

[3] B. Herisse, F.-X. Russotto, T. Hamel, and R. Mahony, "Hovering flight and vertical landing control of a VTOL unmanned aerial vehicle using optical flow," in *Proc. IEEE/RSJ Int. Conf. Intell. Robots Syst. (IROS)*, Sep. 2008, pp. 801–806.

[4] J. R. Azinheira and A. Moutinho, "Hover control of an UAV with back-stepping design including input saturations," *IEEE Trans. Control Syst. Technol.*, vol. 16, no. 3, pp. 517–526, May 2008.

[5] K. U. Lee, Y. H. Yun, W. Chang, J. B. Park, and Y. H. Choi, "Modeling and altitude control of quad-rotor UAV," in *Proc. 11th Int. Conf. IEEE Control, Autom. Syst. (ICCAS)*, Oct. 2011, pp. 1897–1902.

[6] B.-C. Min, J.-H. Hong, and E. T. Matson, "Adaptive robust control (ARC) for an altitude control of a quadrotor type UAV carrying an unknown payloads," in *Proc. 11th Int. Conf. IEEE Control, Autom. Syst. (ICCAS)*, Oct. 2011, pp. 1147–1151.

[7] J. Kim, M.-S. Kang, and S. Park, "Accurate modeling and robust hovering control for a quad–rotor VTOL aircraft," in *Proc. 2nd Int. Symp. UAVs*, Reno, NV, USA, Jun. 2009, pp. 9–26.

[8] J. Stowers, M. Hayes, and A. Bainbridge-Smith, "Altitude control of a quadrotor helicopter using depth map from Microsoft Kinect sensor," in *Proc. IEEE Int. Conf. IEEE Mechatronics (ICM)*, Apr. 2011, pp. 358–362.

[9] N. Guenard, T. Hamel, and V. Moreau, "Dynamic modeling and intuitive control strategy for an 'X4-flyer,'" in *Proc. Int. Conf. IEEE Control Autom. (ICCA)*, vol. 1. Jun. 2005, pp. 141–146.

[10] N. Metni and T. Hamel, "A UAV for bridge inspection: Visual servoing control law with orientation limits," *Autom. Construction*, vol. 17, no. 1, pp. 3–10, 2007.

[11] K. Nonaka and H. Sugizaki, "Integral sliding mode altitude control for a small model helicopter with ground effect compensation," in *Proc. Amer. Control Conf. (ACC)*, Jun. 2011, pp. 202–207.

[12] L. Besnard, Y. B. Shtessel, and B. Landrum, "Control of a quadrotor vehicle using sliding mode disturbance observer," in *Proc. Amer. Control Conf. (ACC)*, Jul. 2007, pp. 5230–5235.

[13] K. Kita, A. Konno, and M. Uchiyama, "Hovering control of a tail-sitter VTOL aerial robot," *J. Robot. Mechatronics*, vol. 21, no. 2, p. 277, 2009.

[14] R. Mahony and T. Hamel, "Robust trajectory tracking for a scale model autonomous helicopter," *Int. J. Robust Nonlinear Control*, vol. 14, no. 12, pp. 1035–1059, Aug. 2004.

[15] H. Li, L. Wu, Y. Li, and C. Li, "Identification of turbine engine dynamics with the governor in the loop," in *Proc. IEEE Int. Conf. Syst., Man, Cybern. (SMC)*, Oct. 2016, pp. 004200–004205.

[16] H. Li, L. Wu, Y. Li, C. Li, and H. Li, "A novel method for vertical acceleration noise suppression of a thrust-vectored VTOL UAV," *Sensors*, vol. 16, no. 12, p. 2054, 2016.

[17] A. A. Mian and W. Daobo, "Nonlinear flight control strategy for an underactuated quadrotor aerial robot," in *Proc. IEEE Int. Conf. Netw., Sens. Control*, Apr. 2008, pp. 938–942.

[18] S. E. Hamamci, "An algorithm for stabilization of fractional-order time delay systems using fractional-order PID controllers," *IEEE Trans. Autom. Control*, vol. 52, no. 10, pp. 1964–1969, Oct. 2007.

[19] G. J. Silva, A. Datta, and S. P. Bhattacharyya, "New results on the synthesis of PID controllers," *IEEE Trans. Autom. Control*, vol. 47, no. 2, pp. 241–252, Feb. 2002.

[20] S. E. Hamamci and M. Koksal, "Calculation of all stabilizing fractional-order PD controllers for integrating time delay systems," *Comput. Math. Appl.*, vol. 59, no. 5, pp. 1621–1629, Mar. 2010.

[21] C. Hwang and J. H. Hwang, "Stabilisation of first-order plus dead-time unstable processes using PID controllers," *IEE Proc.-Control Theory Appl.*, vol. 151, no. 1, pp. 89–94, Jan. 2004.

[22] D. J. Wang and X. L. H. Gao "Design with fractional-order PD controllers," *Automatica*, vol. 48, no. 5, pp. 974–977, 2012.

[23] O. Diekmann *et al.*, *Delay Equations: Functional-, Complex-, and Nonlinear Analysis*. Springer, 2012.

[24] L. S. Pontryagin, "On the zeros of some elementary transcendental functions," *Amer. Math. Soc. Transl.*, vol. 2, no. 1, pp. 95–110, 1955.

[25] W. K. Ho, C. C. Hang, and L. S. Cao, "Tuning of PID controllers based on gain and phase margin specifications," *Automatica*, vol. 31, no. 3, pp. 497–502, 1995.

[26] K.-W. Han, and C.-H. Chang, "Gain margins and phase margins for control systems with adjustable parameters," *J. Guid., Control, Dyn.*, vol. 13, no. 3, pp. 404–408, 1990.

HUANYU LI received the bachelor's degree in electronic engineering from Tsinghua University, China, in 2012, where he is currently pursuing the Ph.D. degree with the Department of Automation. His research interests include flight control for VTOL UAVs.

CHUNWEN LI received the bachelor's and Ph.D. degrees in control science and engineering from Tsinghua University, Beijing, China, in 1982 and 1989, respectively. He is currently a Professor with the Department of Automation, Tsinghua University. His research interests include non-linear control and inverse system control.

HANGYU LI received the bachelor's degree in mechanical engineering from Peking University, China, in 2009, and the master's and Ph.D. degrees in energy resources engineering from Stanford University in 2011 and 2014, respectively. He is currently an Engineer with Shell International Exploration and Production Inc., USA.

YINGJIE LI received the bachelor's degree in flight vehicle propulsion engineering from Beihang University, China, in 2007, and the master's degree in electrical engineering from Tsinghua University, Beijing, China, in 2011, where he is currently pursuing the Ph.D. degree with the Department of Automation. His research interests include flight control and thrust-vectoring control for VTOL UAVs.

ZHIPENG XING received the bachelor's degree in materials physics from the University of Science and Technology, Beijing, China, in 2006, and the master's degree in software engineering from Tsinghua University, Beijing, China, in 2010, where he is currently pursuing the Ph.D. degree with the Department of Automation. His research interests include system identification and data mining.

• • •